INTERNATIONAL JOURNAL FOR NUMERICAL METHODS IN FLUIDS
Int. J. Numer. Meth. Fluids 2006; **52**:925–940
Published online 22 March 2006 in Wiley InterScience (www.interscience.wiley.com). DOI: 10.1002/fld.1212

Viscous flow computations of aircraft with changing control surface deflection using unstructured dynamic meshes

Mitsuhiro Murayama[1,*,†], Yasushi Ito[2,‡], Kazuhiro Nakahashi[3,§], Kisa Matsushima[3,¶] and Toshiyuki Iwamiya[1,‖]

[1]*Institute of Space Technology and Aeronautics, Japan Aerospace Exploration Agency, 7-44-1, Jindaiji Higashi-machi, Chofu, Tokyo 182-8522, Japan*
[2]*Department of Mechanical Engineering, University of Alabama at Birmingham, 1530 3rd Ave S, BEC 352, Birmingham, AL 35294-4461, U.S.A.*
[3]*Department of Aeronautics and Space Engineering, Tohoku University, Aramaki-Aza-Aoba 6-6-01, Sendai 980-8579, Japan*

SUMMARY

A three-dimensional unstructured dynamic mesh method for viscous flow computations is presented to simulate aircraft performance when control surface deflection is changed. The method includes an efficient surface mesh movement algorithm for unstructured hybrid meshes comprised of tetrahedra, prisms and pyramids. The method is applied to numerical simulations of the static longitudinal stability control of an experimental supersonic airplane designed at the Japan Aerospace Exploration Agency (previously known as the National Aerospace Laboratory of Japan). The deflection angles of the horizontal tail wings are changed at freestream Mach numbers of 2.0 and 0.95. The results are validated by comparison with experimental results, and the differences in the flow characteristics at the given flow conditions are estimated. Copyright © 2006 John Wiley & Sons, Ltd.

KEY WORDS: supersonic aircraft; unstructured mesh; aerodynamics; control surface

1. INTRODUCTION

The Japan Aerospace Exploration Agency (previously known as the National Aerospace Laboratory of Japan) has been promoting a supersonic research program since 1996 [1, 2]. The project is developing experimental supersonic airplanes to conduct a basic study for

*Correspondence to: Mitsuhiro Murayama, Institute of Space Technology and Aeronautics, Japan Aerospace Exploration Agency 7-44-1, Jindaiji Higashi-machi, Chofu, Tokyo 182-8522, Japan.
†E-mail: murayama.mitsuhiro@jaxa.jp
‡E-mail: yito@uab.edu
§E-mail: naka@ad.mech.tohoku.ac.jp
¶E-mail: kisam@ad.mech.tohoku.ac.jp
‖E-mail: iwamiya.toshiyuki@jaxa.jp

Received 21 January 2004
Revised 26 January 2006
Accepted 27 January 2006

the next generation commercial supersonic transport. In this program, an un-manned non-powered experimental supersonic airplane, *N*ational *EX*perimental *S*upersonic *T*ransport (NEXST-1), has been developed and the flight test will be conducted soon. This airplane was designed to cruise at Mach 2.0. As its design concepts, a cranked arrow, modulated warp, natural laminar flow wing and an area-ruled body were employed to achieve a high lift-to-drag ratio. To design such an advanced airplane, Computational Fluid Dynamics (CFD) is expected to play an important role.

To build a safe airplane, the precise prediction of flow characteristics during manoeuvres is essential. One of the most important issues in manoeuvring is the stability control of the longitudinal airplane motion. The aerodynamic characteristics have to be estimated under various flight conditions and expected deflection angles of control surfaces. Furthermore, trim is important for dynamic stability control. We need to know the dynamic response of an airplane when the control surfaces are changed abruptly. However, wind tunnel experiments to obtain such data are extremely difficult. At present, an expensive flight test only can bring precise understanding of flow characteristics when an airplane is being manoeuvred. Thus, CFD holds great promise for solution of this type of dynamic response problem as well as for clarification of the static response.

To simulate such response problems, CFD must have a capability to model actual complex airplanes. In addition, the computational meshes need to be moved/deformed to accompany the movement and deformation of its control surfaces and the airplane itself.

In general, a dynamic mesh method would be a candidate to treat this problem. It is, however, not straightforward to treat control surfaces whose movable parts are closely located near the fuselage, such as all moving tail wing for high-speed aircraft. NEXST-1 adopted the all moving tail wing as a longitudinal control surface. If narrow space is opened between the fuselage and the control surfaces, a number of mesh points are required near the space. In addition, ill-conditioned cells may be easily generated due to the mesh movement. On the other hand, if the control surfaces move along the fuselage without the narrow space, the intersecting part between the control surfaces and fuselage is changed due to the deflection angle of the control surfaces. Therefore, surface mesh points of the fuselage also have to be moved while maintaining the original curved surface of the fuselage due to the change of the intersection. However, it is difficult to directly move the surface mesh points along the curved surface without changing the original mesh topology and geometry.

To simulate aircraft performance when control surface deflection is changed, we have been developing an efficient unstructured dynamic mesh method incorporating surface mesh movement algorithm to treat the change of the deflection angle of the control surface [3–5]. The method was applied to numerical simulations of control surface response of NEXST-1. Inviscid flow computations around the airplane were performed with change in the control surface deflection and the validation of the results has been confirmed by comparison to experimental data [5]. Moreover, a simulation system has been constructed to estimate the unsteady response of the airplane's motion to the deflection angle of the control surface and the possibility of dynamic flight control simulation has been shown [5].

The unstructured dynamic mesh method has shown its capability. However, it is for inviscid flow simulations using unstructured tetrahedral meshes. The aerodynamic forces have to be estimated under various flight conditions. The influence of the viscosity becomes larger in the transonic and subsonic flow fields. Recently, an airplane that cruises near sonic regime has attracted international attention. In the near sonic regime, however, the aerodynamic

characteristics of an airplane have not been well understood yet, especially with regards to control surface deflection. In this paper, the previous computational techniques are extended to computations of viscous flows and applied to viscous flow simulations of the longitudinal stability control of NEXST-1. Computations are performed changing the deflection angles of the control surface at the cruising Mach number, $M_\infty = 2.0$ and a near sonic Mach number, $M_\infty = 0.95$ and the differences in the flow characteristics at the given flow conditions are estimated.

2. MESH POINT MOVEMENT METHOD

In our previous studies, a dynamic mesh method has been applied to unstructured tetrahedral meshes [3–5]. The method is based on the linear tension spring analogy [6]. It is now extended to accept unstructured hybrid mesh composed of tetrahedral, prisms, and pyramids.

Edges of the elements are modelled as linear tension springs. The force $\mathbf{F}_{\text{spring}\,ij}$ is exerted on a spring when mesh points move

$$\mathbf{F}_{\text{spring}\,ij} = k_{\text{spring}\,ij}\Delta\mathbf{x}_{ij} \tag{1}$$

where $k_{\text{spring}\,ij}$ is the spring stiffness coefficient at edge ε_{ij} and $\Delta\mathbf{x}_{ij}$ is the change in distance between points i and j. The static equilibrium equations, Equation (2), of these forces are solved iteratively at each interior node and the displacements in x, y, and z directions are determined.

$$\sum_{j\in\varepsilon_{ij}} \mathbf{F}_{\text{spring}\,ij} = 0 \tag{2}$$

Here, mesh points on the outer boundary of the mesh are fixed and the displacements on the body surface are given as the initial conditions. By use of the edge length l_{ij} as the spring stiffness described in Equation (3), the method can prevent each vertex from colliding with the other

$$k_{\text{spring}\,ij} = 1/l_{ij} \tag{3}$$

To improve the robustness of the dynamic mesh method, treatment specific to cell types and shapes is considered. For prisms and pyramids generated near no-slip wall boundaries, the spring stiffness of the edges that compose the prisms and pyramids is much enhanced by the wall distance function $f_d \propto 1/d$. The function is multiplied to the spring stiffness coefficients to suppress the deformation of the mesh near the wall and to keep its original clean shape. This function allows the elements near the walls to be nearly rigidly moved.

To generate hybrid meshes for three-dimensional high Reynolds number viscous flow computations, TAS_MESH [7–9] is employed. A hybrid mesh is generated from an isotropic tetrahedral mesh as an initial background mesh to enhance the robustness.

In the mesh generation method, the surface mesh is comprised of triangles. First, an isotropic tetrahedral mesh is generated as an initial background mesh using the triangular surface mesh. The tetrahedra near no-slip wall boundaries are shifted gradually to accommodate each prismatic layer. Prisms are then added near the walls while preserving the mesh validity. The gap between the prisms and tetrahedra is filled with pyramids. Although the volume mesh has

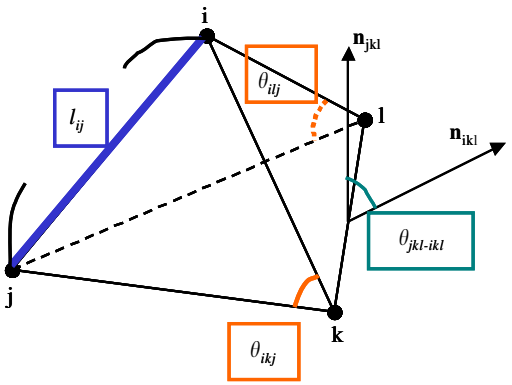

Figure 1. Determination of spring coefficients at a tetrahedron.

hybrid structure, the surface mesh is still comprised of triangles. Nowadays, isotropic tetrahedral meshes for computations of inviscid flows and low Reynolds number viscous flows can be generated around highly complex geometries with high levels of robustness [7]. By using an isotropic tetrahedral mesh as a background mesh for the hybrid mesh generation, the mesh validity can be checked beforehand and the mesh quality is easily controlled.

The resulting method has shown its capability to generate hybrid meshes for highly complex configurations without user-intervention and the computed results have been validated against experiment [8, 9]. While, the method may generate ill-conditioned flat tetrahedral elements near prismatic elements, the flat tetrahedral elements may easily turn into invalid elements that have negative volume due to mesh movement. To prevent this failure, therefore, the geometry of tetrahedral elements should be considered.

Figure 1 shows a tetrahedral element. In this study, to prevent each triangular face that constructs the tetrahedral element from being flat or inverted, the internal angles of triangles, which share the edge ε_{ij}, are considered. Moreover, to prevent the tetrahedral volume from becoming zero or negative, the angles between two faces, $\theta_{jkl-ikl}$, between the faces ikl and jkl, are considered. The spring coefficients at the edge ε_{ij} are determined as follows:

$$k_{\text{angle } ij} = \sum \frac{1}{\sin^2 \theta} \tag{4}$$

$$k_{ij} = k_{\text{spring } ij} + k_{\text{angle } ij} \tag{5}$$

Because $k_{\text{angle } ij} \to \infty$ when $\theta \to \pi$ or 0, the spring prevents the cells from being flat or inverted and having zero or negative area.

3. SURFACE MESH MOVEMENT

For the simulation of an airplane's response to control surface deflection, the surface mesh on the fuselage near the fuselage-control wing junction has to be moved according to the movement of the control wing. However, to move the surface mesh while maintaining the

original curved surface is difficult, because no straightforward information is provided about the original surface curvature. There is information only on discrete mesh points. In other words, it is difficult to directly move the surface mesh points along the curved surface in a proper manner.

Here, a surface mapping moving mesh method [3–5] developed by the authors is used, in which mapping of the surface component onto a two-dimensional parameter domain is applied. This idea is similar to the algorithm for generating unstructured surface meshes [10]. A portion of three-dimensional surface mesh is cut out and mapped onto a two-dimensional parameter domain. The moving mesh method discussed in the previous section is then applied in the parameter domain. The moved mesh is transformed back onto the three-dimensional domain. By this method [3–5], the control surface can be moved smoothly.

4. FLOW SOLVER

As the mesh generator and the flow solver, *T*ohoku University *A*erodynamic *S*imulation code (TAS code) is used in this study.

The original unstructured surface mesh, tetrahedral volume mesh for computations of inviscid flows, and hybrid volume mesh composed of tetrahedra, prisms, and pyramids for high Reynolds number viscous flows are generated by TAS_MESH [7–9, 11, 12].

The flow fields are computed by TAS_Flow. In TAS_Flow, the Navier–Stokes equations are solved on the unstructured mesh by a finite volume cell–vertex scheme. The control volumes are non-overlapping dual cells constructed around each node. The Harten–Lax–van Leer–Einfeldt–Wada Riemann solver (HLLEW) [13] is used for the numerical flux computations. Second-order spatial accuracy is realized by a linear reconstruction of the primitive variables. LU-SGS implicit method for unstructured meshes [14] is used for the time integration. A one-equation turbulence model by Goldberg and Ramakrishnan [15] is implemented to treat turbulent boundary layers for computations of viscous flows.

5. RESULTS

Viscous flow simulations of the longitudinal stability control of NEXST-1 were carried out using the three-dimensional dynamic mesh method for hybrid unstructured meshes and surface dynamic mesh method.

Figure 2 shows the hybrid mesh for viscous flow computations of the NEXST-1, which contains 922 489 nodes, 1 146 337 tetrahedra, 1 376 088 prisms, and 31 525 pyramids. Parameters for adding the prismatic layers were as follows: the number of layers is 25, the minimum spacing in the normal direction to the wing surface of $0.05/\sqrt{Re}$ and the stretching factor of 1.2. At the sharp corners such as the wing trailing edge, double normal vectors were employed to enhance the mesh quality as shown in Figure 2(d). Computations were performed with a change in the deflection angle of the horizontal tail wing. Freestream Mach numbers, M_∞, of 2.0 and 0.95 were employed. Reynolds numbers based on the full length of the 8.5% scaled wind tunnel model are 26.9×10^6 at $M_\infty = 2.0$ and 10.7×10^6 at $M_\infty = 0.95$. The full length of the model is 0.9775 (m). All turbulent flows were assumed in the computations.

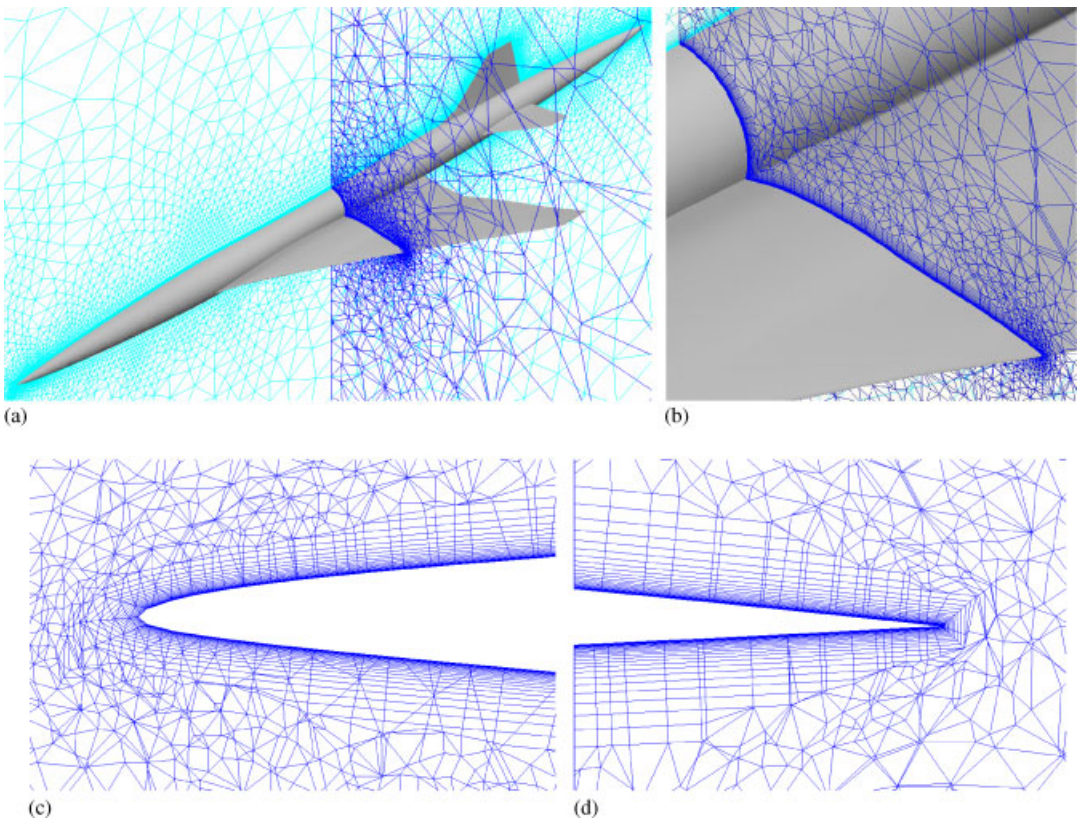

Figure 2. Hybrid mesh for viscous flow computations of an experimental supersonic airplane of the National Aerospace Laboratory of Japan (NEXST-1): (a) full view of the aircraft; (b) close-up view of a cross flow section; (c) leading edge of the main wing at a semi-span station; and (d) trailing edge of the main wing at a semi-span station.

Computed results are compared with experimental results and computed results of inviscid flows in our previous work [5]. The wind tunnel experimental model had a sting at the tail. The integrated aerodynamic coefficients were evaluated except for the sting. For the inviscid flow computations, a tetrahedral computational mesh was employed, which contained 208 732 nodes, 1 114 365 tetrahedra.

The process of the surface mesh movement in the computations is shown in Figures 3–7. In our computational meshes, the surface mesh is comprised of triangles. The horizontal tail wing is moved, so that the deflection angle is changed from 0° to 5°. First, the junction between the fuselage and tail surface is determined and a portion of the surface mesh near the junction is cut out as shown in Figure 3. Then, a fine regular patch mesh along the curved fuselage surface is constructed and linear interpolation is used to transfer data between the surface mesh and the patch mesh. The regular patch mesh is easily transformed onto a two-dimensional parameter domain. The three-dimensional unstructured surface mesh is then transformed onto the parameter domain based on the formulated interpolation. The transformation of the surface

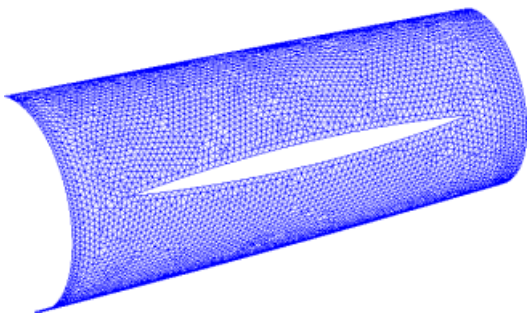

Figure 3. A portion of fuselage surface mesh around the horizontal tail wing.

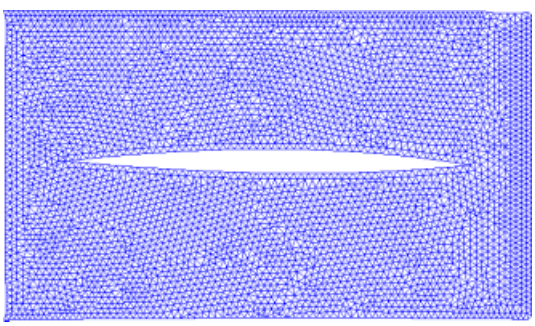

Figure 4. Surface mesh transformed onto a two-dimensional parameter domain.

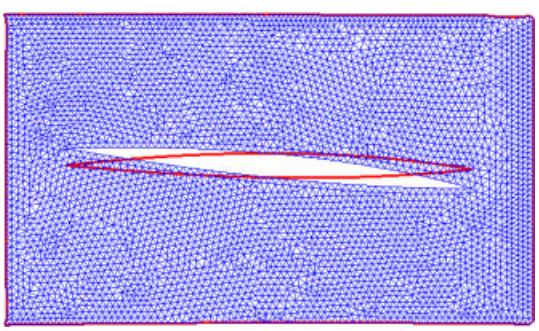

Figure 5. Surface mesh moved in the parameter domain.

mesh onto the two-dimensional parameter domain is shown in Figure 4. The moving mesh method is then applied in the parameter domain shown in Figure 5. Again, interpolation information is formulated after the mesh movement and the moved mesh is then transformed back onto the three-dimensional domain as shown in Figure 6. Finally, the hybrid volume

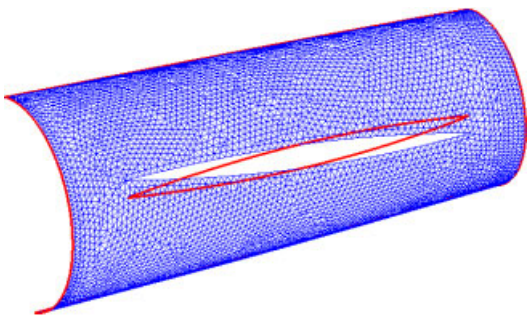

Figure 6. Surface mesh transformed back onto the three-dimensional domain.

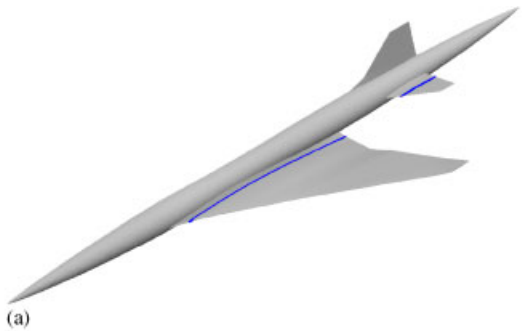

(a)

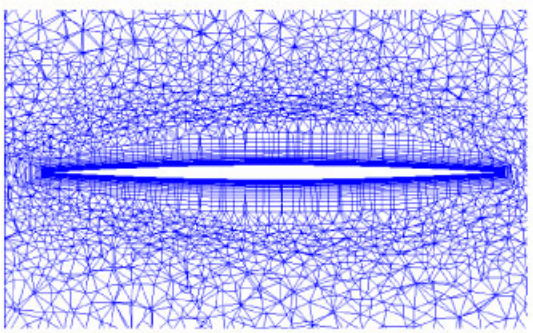

(b)

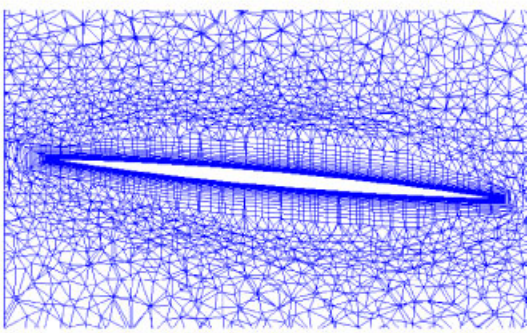

(c)

Figure 7. Change in the deflection angle of the horizontal tail wing: (a) aircraft geometry; (b) cross-sectional view of mesh around tail wing before movement; and (c) after movement (The cross section is indicated as lines in (a)).

mesh is moved according to the surface mesh movement using the method described in the previous section as shown in Figure 7. Figures 7(b) and (c) show cross-sectional views of the mesh around the tail wing before/after mesh movement. The cross-section is indicated as lines in Figure 7(a).

In changing the deflection angle of the horizontal tail wing, the surface configuration of the airplane must usually be re-defined using CAD, and the surface mesh must be re-generated. Then, the computational volume mesh is re-generated and the computation is performed. Repeating the process of generating the surface configuration and surface/volume mesh is a time-consuming task, which takes several hours by a skilled engineer in this case. By the surface/volume mesh movement method, this process can be easily and automatically conducted in just several minutes. Hence, with the proposed method, the aerodynamic forces resulting from the change of both the angle of attack and the deflection angle of the horizontal tail wing can be estimated efficiently, and unsteady analysis can also be conducted at much lower cost and manpower.

Figures 8 and 9 show the computed Mach number contours estimated from viscous and inviscid flows at $M_\infty = 2.0$ and 0.95. Compared with the computed results of inviscid flows, those of viscous flows show some differences in the wake of the main wing. The lower surface of the horizontal tail wing is influenced by the wake. Figures 10 and 11 show the surface pressure coefficients of the tail wing at a semi-span station shown in Figure 7(a). At $M_\infty = 2.0$, the differences of the surface pressure coefficients between the viscous flow computations (NS) and inviscid flow computations (Euler) are small. On the other hand, at $M_\infty = 0.95$, the differences between NS and Euler become larger. Especially in the case of $M_\infty = 0.95$ and deflection angle of 5.0°, locations of the shock wave on the tail wing are different and moved relatively upstream in NS.

For the code validation, the variations of the aerodynamic coefficients due to the change of the angle of attack of the whole body are shown in Figure 12. As for lift and pitching moment coefficients, although there are slight discrepancies at low angles of attack at $M_\infty = 0.95$, the computational results show good agreement with the experimental results at both Mach numbers as shown in Figures 12(a) and (b). As for drag coefficients as shown in Figure 12(c), the computational results at $M_\infty = 2.0$ show reasonable agreement with experimental results, while the computational results at $M_\infty = 0.95$ overpredict the drag coefficients by about 30–50 counts (1 count $= 1.0 \times 10^{-4}$). At higher angles of attack, the discrepancy becomes relatively larger due to the effect of the separation induced by leading-edge vortices.

In the experimental results at $M_\infty = 0.95$, the effect of the sting and the wall of the wind tunnel is significant. In Reference [16], their effects on the wind tunnel model are discussed based on CFD simulations. It was reported that the surface pressure distributions on the main wing were largely influenced by the sting and the wind tunnel wall. It results in drag discrepancy about 10–20 counts at the tested angles of attack. Therefore, the computational results at moderate angles of attack are thought to be reasonable, although further validation is required.

The variations of the aerodynamic coefficients due to the deflection angles of the horizontal tail wing are shown in Figure 13. In the experiments, the lift and pitching moment coefficients have been measured only at the deflection angles of $-10°, 0°$, and 10°. The data at other deflection angles are linearly interpolated from the three points. The computational results at various deflection angles of the horizontal tail wing agree well with the experimental results. The validity of the method using the dynamic mesh method for hybrid unstructured meshes is apparent. Compared with Euler results, the lift and moment coefficients by NS show better agreement with experiments.

From Figure 13, the lift and pitching moment coefficients are linearly influenced by the change of the deflection angles of the tail wing and no discontinuity can be seen even at

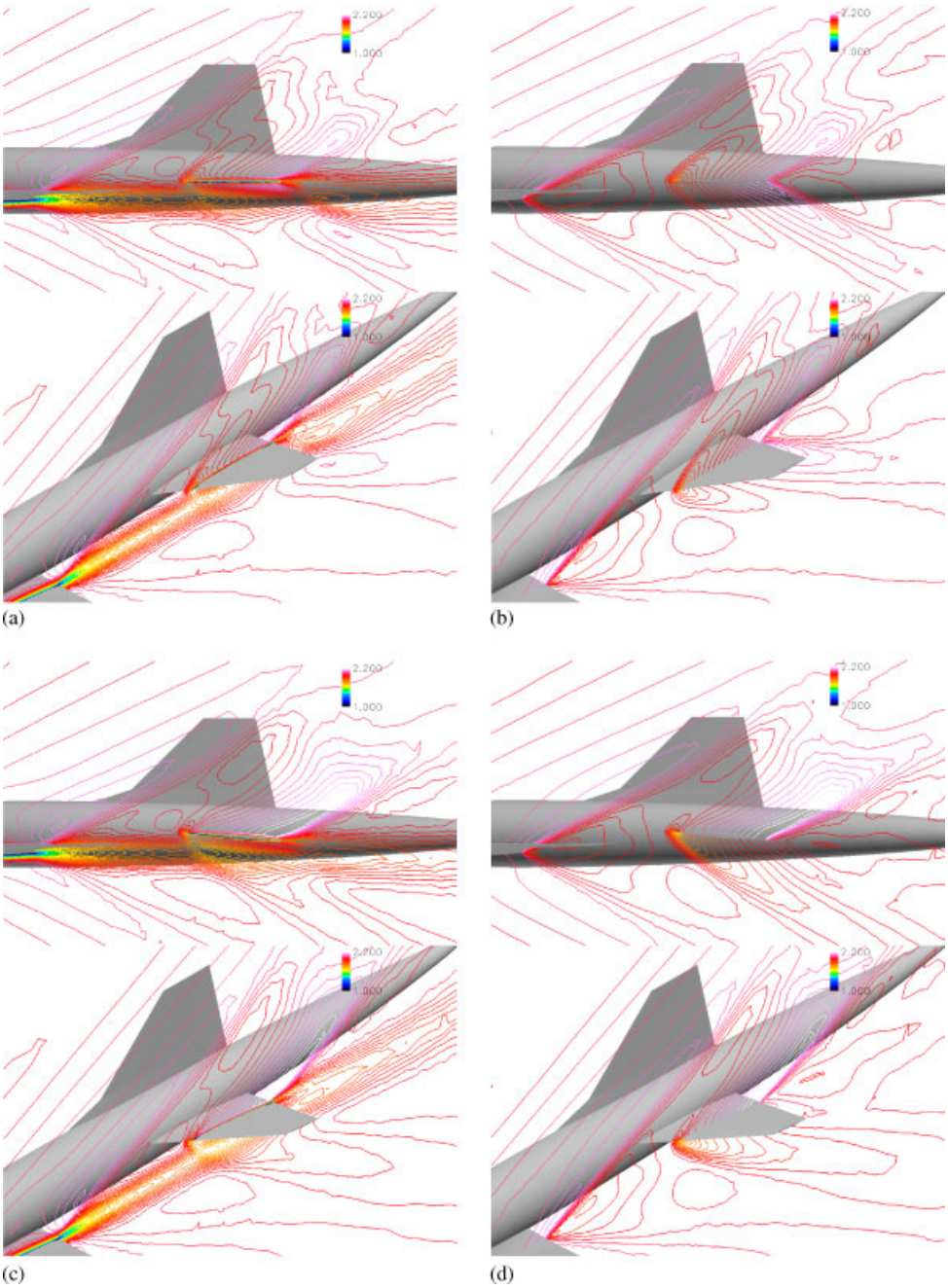

Figure 8. Mach number contours ($M_\infty = 2.0$); β: deflection angle of the tail wing: (a) NS computation ($\beta = 0.0$); (b) Euler computation ($\beta = 0.0$); (c) NS computation ($\beta = 5.0$); and (d) Euler computation ($\beta = 5.0$).

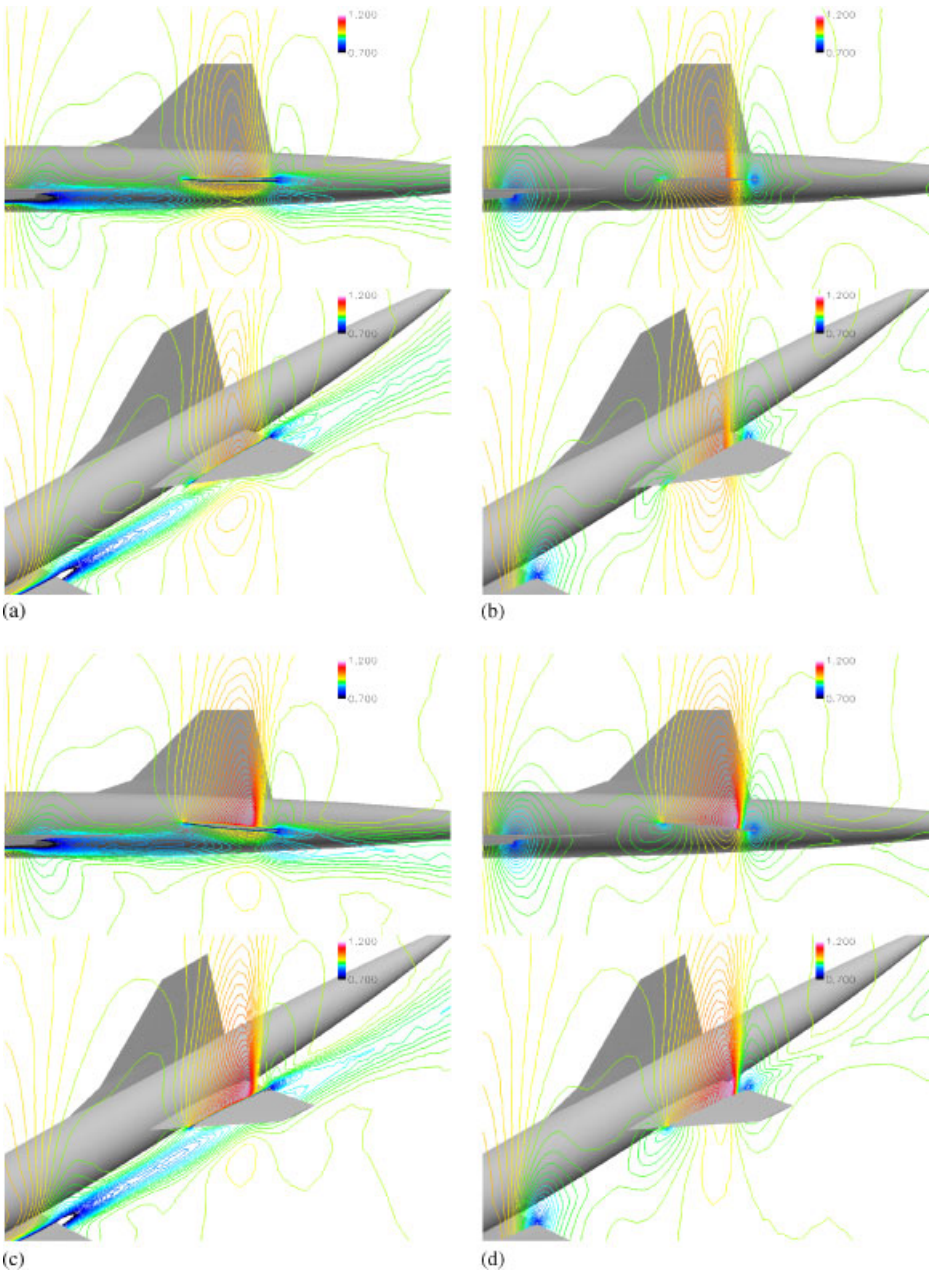

Figure 9. Mach number contours ($M_\infty = 0.95$); β: deflection angle of the tail wing: (a) NS computation ($\beta = 0.0$); (b) Euler computation ($\beta = 0.0$); (c) NS computation ($\beta = 5.0$); and (d) Euler computation ($\beta = 5.0$).

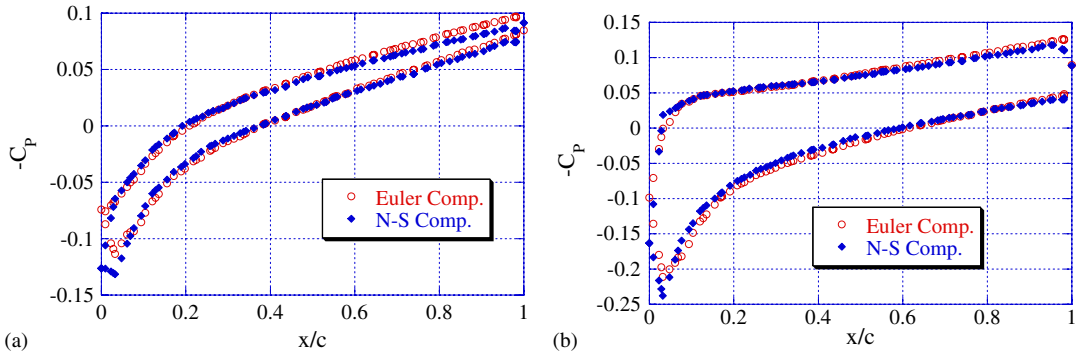

Figure 10. Surface pressure coefficients of the tail wing at $z/c = 0.035$ ($M_\infty = 2.0$); β: deflection angle of the tail wing: (a) $\beta = 0.0$; and (b) $\beta = 5.0$.

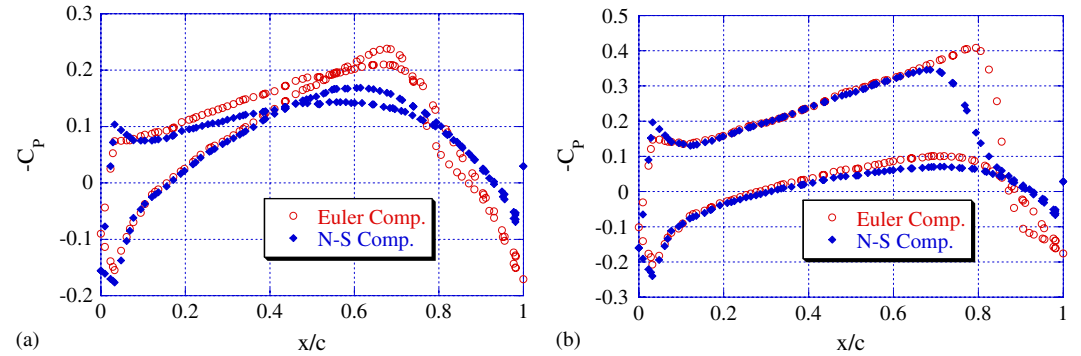

Figure 11. Surface pressure coefficients of the tail wing at $z/c = 0.035$ ($M_\infty = 0.95$); β: deflection angle of the tail wing: (a) $\beta = 0.0$; and (b) $\beta = 5.0$.

$M_\infty = 0.95$. As for the lift and pitching moment coefficients at these Mach numbers, the assumption of linear interpolation using the three points is proven to be valid.

Compared with the results at $M_\infty = 2.0$ and 0.95 in Figure 13, the slope of the aerodynamic coefficients at $M_\infty = 0.95$ is much larger. The coefficients of the main wing are not much influenced by the deflection angle even at $M_\infty = 0.95$. In the case of $M_\infty = 0.95$, the locations and strength of the shock wave on the tail wing are significantly influenced by the deflection angle, as shown in Figure 9. Moreover, the shock wave on the tail wing influences the aerodynamic forces on the fuselage. Therefore, the overall effect on aerodynamic coefficients at $M_\infty = 0.95$ is larger than at $M_\infty = 2.0$.

Figures 14 and 15 show the variation of the hinge moment coefficients of the tail wing due to the change of the deflection angle of the tail wing $M_\infty = 2.0$ and 0.95, respectively. The hinge moment coefficients are evaluated at several constant angles of attack. Measurement of the hinge moments in the wind tunnel is troublesome, but the data is very important for

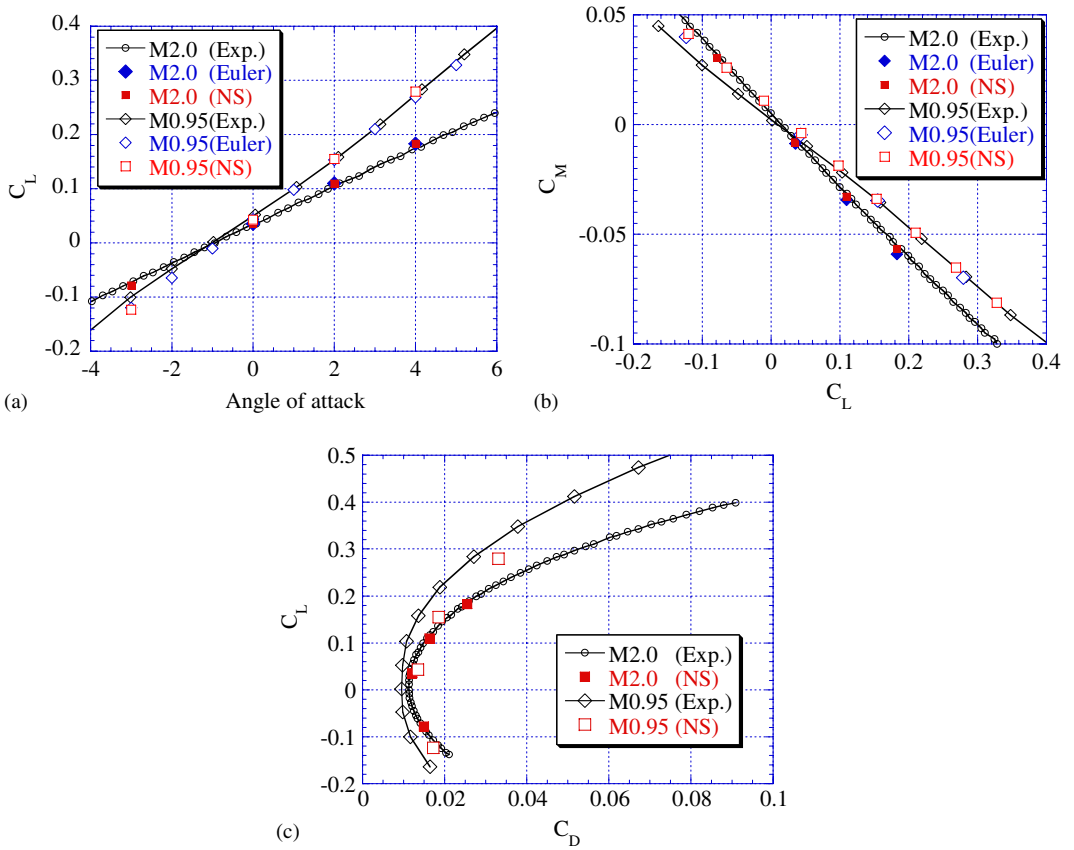

Figure 12. Variations of the lift coefficients (C_L), pitching moment coefficients (C_M), and drag coefficients (C_D) due to the angle of attack of the wing-fuselage (α) (Deflection angle of the horizontal tail wing is zero.): (a) $C_L - \alpha$; (b) $C_M - C_L$; and (c) $C_L - C_D$.

control of the longitudinal motion. Therefore, the estimation from numerical simulations will be very helpful.

In Figure 14, the hinge moment coefficients are linearly influenced due to the deflection angle of the tail wing at $M_\infty = 2.0$. At $M_\infty = 2.0$, the inviscid and viscous flow computations give nearly the same results. It shows fair agreement with experimental results, but the slopes of the experimental results are a little steeper than that of the computational results and the discrepancies become larger at higher/lower deflection angles.

In Figure 15, the computational results are in fair agreement with the experimental results. However, a different tendency can be seen by comparison with the results at $M_\infty = 2.0$. At $M_\infty = 0.95$, the hinge moment coefficients are non linear with respect to the variation in deflection angles in both inviscid and viscous flow computations. The discrepancies between the results of inviscid and viscous flow computations can also be seen. At this Mach number the shock wave is generated on the tail wing, and the locations and strength of the shock

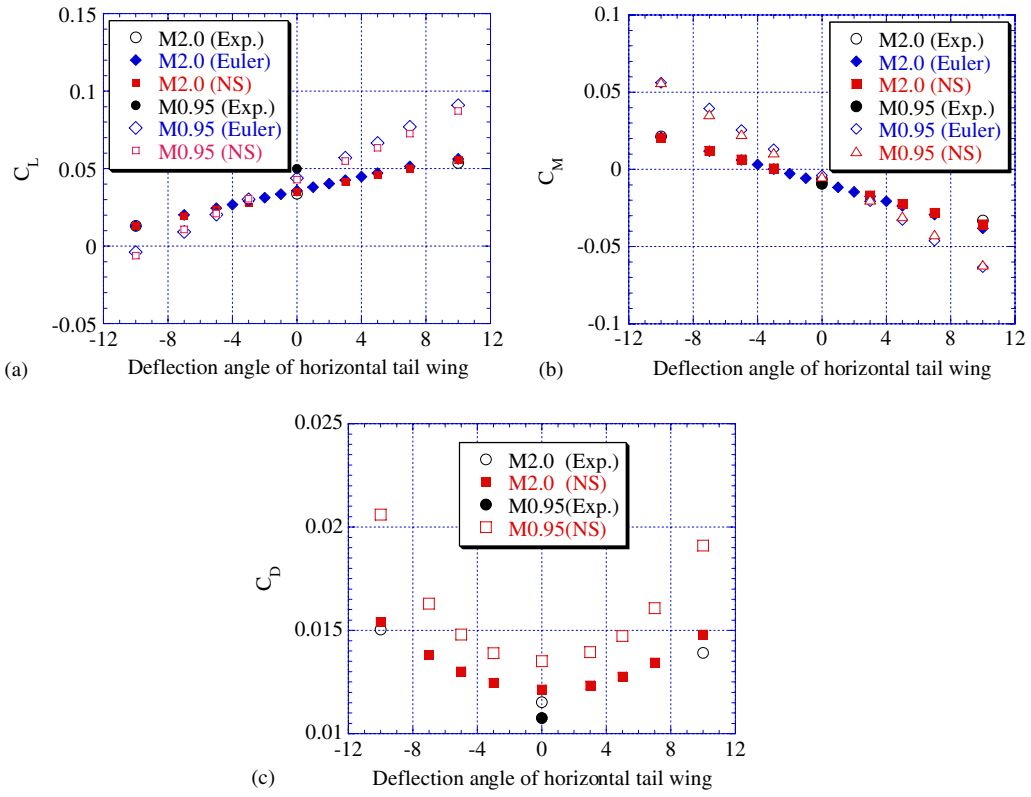

Figure 13. Variations of the lift coefficients (C_L), pitching moment coefficients (C_M), and drag coefficients (C_D) due to the deflection angle of the horizontal tail wing (β): (a) $C_L - \beta$; (b) $C_M - \beta$; and (c) $C_D - \beta$.

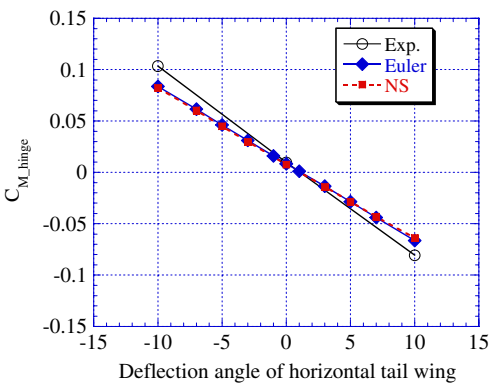

Figure 14. Variation of the hinge moment coefficients (C_M_hinge) with respect to deflection angle of horizontal tail wing (β) at $M_\infty = 2.0$.

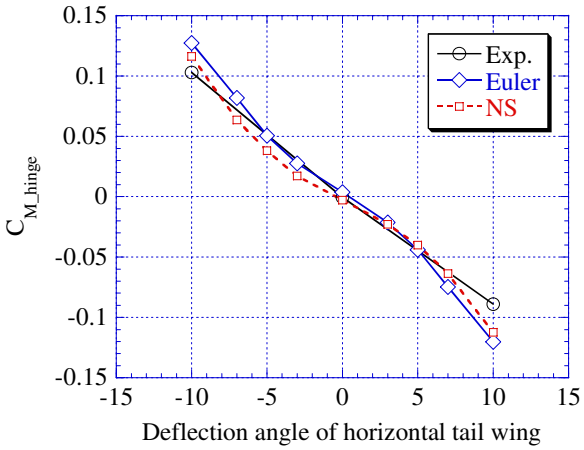

Figure 15. Variation of the hinge moment coefficients (C_{M}_hinge) with respect to deflection angle of horizontal tail wing (β) at $M_\infty = 0.95$.

wave on the tail wing are greatly affected by the deflection angle. Thus, the shock wave may influence the prediction of the hinge moment. In the experimental results, however, the hinge moment coefficients are measured only at the deflection angles of $-10°$, $0°$, and $10°$. Further investigations will be required in both the computations and the experiments.

6. CONCLUSION

A three-dimensional dynamic mesh method with surface mesh movement for unstructured hybrid meshes has been developed for viscous flow computations of the aircraft response to control surface deflection. The method was applied to the numerical simulation of control surface response for an experimental supersonic airplane (NEXST-1). The viscous flow fields at freestream Mach numbers, M_∞, of 2.0 and 0.95 with change in the deflection angle of the horizontal tail wing were evaluated.

Using the method, the aerodynamic forces resulting from the change of deflection angle of the control surface were estimated efficiently. Compared with the computed results of inviscid flows, the lower surface of the horizontal tail wing was influenced by the wake in the viscous flow computations. In the case of $M_\infty = 0.95$ and deflection angle of $5.0°$, the location of the shock wave on the tail wing was different and moved relatively upstream.

Variations of the aerodynamic coefficients due to the deflection angle at $M_\infty = 0.95$ were larger than those at $M_\infty = 2.0$. This is because a shock wave is present on the tail wing in the case of $M_\infty = 0.95$. The locations and strength are significantly affected by the deflection angle. This affects the aerodynamic forces on the tail wing and the fuselage.

Computed lift, pitching moment, drag, and hinge moment coefficients showed reasonable agreement with experimental results. Lift, pitching moment, and hinge moment coefficients were almost linearly affected by the change of the deflection angle of the tail wing, except for the hinge moment at $M_\infty = 0.95$. At $M_\infty = 0.95$, the shock wave on the tail wing was

a strong function of the deflection angle. The shock wave may influence the prediction of the hinge moment.

REFERENCES

1. Iwamiya T. A computational study on unmanned scaled supersonic experimental airplane. *AIAA Paper 2002-2841*, 2002.
2. Yoshida K, Makino Y, Shimbo, Y. An experimental study on unmanned scaled supersonic experimental airplane. *AIAA Paper 2002-2842*, 2002.
3. Murayama M, Nakahashi K, Matsushima K. Unstructured dynamic mesh for large movement and deformation. *AIAA Paper 2002-0122*, 2002.
4. Murayama M, Nakahashi K, Matsushima K. A simple and robust unstructured dynamic mesh method with surface grid movement. *Proceedings of 8th International Conference on Numerical Grid Generation in Computational Field Simulations*, Honolulu, U.S.A., 2002.
5. Murayama M, Togashi F, Nakahashi K, Matsushima K, Kato T. Simulation of aircraft response to control surface deflection using unstructured dynamic grids. *Journal of Aircraft* 2005; **42**(2):340–346.
6. Batina JT. Unsteady Euler algorithm with unstructured dynamic mesh for complex—aircraft aerodynamic analysis. *AIAA Journal* 1991; **29**(3):327–333.
7. Sharov D, Nakahashi K. A boundary recovery algorithm for delaunay tetrahedral meshing. *Proceedings of 5th International Conference on Numerical Grid Generation in Computational Field Simulations*, 1996, 229–238.
8. Ito Y, Nakahashi K. Unstructured hybrid grid generation based on isotropic tetrahedral grids. *AIAA Paper 2002-0861*, 2002.
9. Ito Y, Nakahashi K. Improvements in the reliability and quality of unstructured hybrid mesh generation. *International Journal for Numerical Methods in Fluids* 2004; **45**(1):79–108.
10. Morgan K, Peraire J, Peiro J. Unstructured grid methods for compressible flows. *AGARD-R-787*, 1992.
11. Ito Y, Nakahashi K. Direct surface triangulation using stereolithography data. *AIAA Journal* 2002; **40**(3): 490–496.
12. Ito Y, Nakahashi K. Surface triangulation for polygonal models based on CAD data. *International Journal for Numerical Methods in Fluids* 2002; **39**(1):75–96.
13. Obayashi S, Guruswamy GP. Convergence acceleration of an aeroelastic Navier–Stokes solver. *AIAA Journal* 1995; **33**(6):1134–1141.
14. Sharov D, Nakahashi K. Reordering of hybrid unstructured grids for lower–upper symmetric Gauss–Seidel computations. *AIAA Journal* 1998; **36**(3):484–486.
15. Goldberg UC, Ramakrishnan SV. A pointwise version of Baldwin–Barth turbulence model. *Computational Fluid Dynamics* 1993; **1**:321–338.
16. Takenaka K, Nakao M, Yamamoto K, Takaki R. Flow analysis and its validation of NEXST-1 near Mach 1. *Proceedings of the 16th Symposium on Computational Fluid Dynamics*, Tokyo, Japan, December 2001 (in Japanese).

